Out-of-time ordered correlators and entanglement growth in the random-field XX spin chain

Jonathon Riddell* and Erik S. Sørensen†
Department of Physics & Astronomy, McMaster University 1280 Main St. W., Hamilton, Ontario, Canada L8S 4M1

(Received 7 October 2018; revised manuscript received 20 December 2018; published 13 February 2019)

We study out-of-time ordered correlations $C(x,t)$ and entanglement growth in the random-field XX model with open boundary conditions using the exact Jordan-Wigner transformation to a fermionic Hamiltonian. For any nonzero strength of the random field, this model describes an Anderson insulator. Two scenarios are considered: a global quench with the initial state corresponding to a product state of the Néel form, and the behavior in a typical thermal state at $\beta = 1$. As a result of the presence of disorder, the information spreading as described by the out-of-time correlations stops beyond a typical length scale ξ_{OTOC}. For $|x| < \xi_{\mathrm{OTOC}}$, information spreading occurs at the maximal velocity $v_{\max} = J$ and we confirm predictions for the early-time behavior of $C(x,t) \sim t^{2|x|}$. For the case of the quench starting from the Néel product state, we also study the growth of the bipartite entanglement, focusing on the late- and infinite-time behavior. The approach to a bounded entanglement is observed to be slow for the disorder strengths we study.

DOI: 10.1103/PhysRevB.99.054205

I. INTRODUCTION

A recent conjecture [1] establishing a bound for the rate of growth of chaos in quantum systems has spurred interest in the study correlators of the form [2]

$$C(x,t) = \langle [W(x,t), V(0)]^{\dagger} [W(x,t), V(0)] \rangle, \tag{1}$$

where W and V are local nonoverlapping operators separated by a displacement x, $[W(x,0), V(0)] = 0$, and $\langle \cdot \rangle$ is a thermal average. If W, V are both Hermitian and unitary, it follows that

$$C(x,t) = 2(1 - \mathrm{Re}[F(x,t)])$$

with $F(x,t) = \langle W(x,t)V(0)W(x,t)V(0) \rangle$ and F is therefore referred to as an out-of-time ordered correlator (OTOC). While W and V commute at $t = 0$, this may no longer be the case at a later time giving rise to the notion of a growing "operator radius" [3] defined as the distance $R_W(t)$, where $F(x,t)$ significantly deviates from 1 for all $|x| < R_W(t)$. $C(x,t)$ can then be seen as a measure of the degree of noncommutativity of $W(x,t)$ and $V(0)$ for $t > 0$, and if $C(x,t)$ remain large for an extended period of time the system is said to be scrambled. From a state perspective the function $F(x,t)$ describes the process of acting with the local operator V on the state, time evolving to some time t and acting on the state with W some displacement x away, and the overlap it has with the state where these operations are inverted. In a chaotic system, this overlap should decay in time to zero [4].

The time where $C(x,t)$ becomes $O(1)$ defines a "scrambling" time t_*, and for the early-time approach to scrambling it is expected that for some models $C(0,t) \sim e^{\lambda_L t}$ with the conjectured [1] bound $\lambda_L \leqslant 2\pi k_B T/\hbar$. Systems that approach this bound are known as fast scramblers [5–10]. This is in contrast to a range of models that do not exhibit this early-time exponential growth [3,4,11–15] and are therefore known as slow scramblers. In particular, OTOCs in many-body localized systems [16,17] (MBL) have been studied [3,4,12–14,18–21] and early-time power-law growth of $C(x,t)$ is expected [3,4,12,14] in such systems. distinguishing them from Anderson localized (AL) models where $C(x,t)$ is expected to be a constant [14], at least for very strong disorder. The behavior of the correlator $C(x,t)$ is therefore capable of distinguishing different phases.

More generally, if the spatial dependence is taken into account, $C(x,t)$ exhibits the butterfly effect [22–24] with certain models exhibiting the behavior $C \sim e^{\lambda_L(t - x/v_B)}$. Here, v_B is the butterfly velocity that can be viewed as the velocity of information in a strongly correlated systems. Perturbative weak coupling calculations [24,25] recover similar exponential behavior, whereas random circuit models [26–28] show a diffusively spreading $C \sim e^{-\lambda_L (x - v_B t)^2/t}$, and for noninteracting translationally invariant systems it can be shown that [19,20] $C \sim e^{-\lambda_L (x - v_B t)^{3/2}/t^{1/2}}$. A universal form has also been proposed [20]:

$$C(x,t) \sim \exp\left(-\lambda_L \frac{(x - v_B t)^{1+p}}{t^p}\right). \tag{2}$$

It should be noted that these different forms are only expected to be valid close to the "wave front," where $x - v_B t$ is small. We also note that, in general, v_B can be different from v_E [29], the rate at which entanglement spreads, but for the models we shall consider here $v_B = v_E$ [30].

Recent studies [14,30] have also shown that $C(x,t)$ can be directly related to the second Rényi entropy $S^{(2)}$ of an appropriately defined subsystem, and scrambling in a quantum channel can be defined in terms of the tripartite information of a subsystem [30]. The quasiprobability behind the OTOC [31–33] has also been studied.

The closely related concept of the growth of entanglement after a quench has been intensely studied with the observation of a logarithmic growth with time [15,34–37] as one of the hallmark features of MBL. In contrast, a thermal phase should

*riddeljp@mcmaster.ca
†sorensen@mcmaster.ca

exhibit linear growth of the entanglement and in the AL phase a bounding constant entanglement is expected [14,38–42].

The relationship between scrambling, the OTOC, and thermalization has also been considered [43–45]. Models which can be mapped to a quasi-free-fermionic model with delocalizing dynamics have been studied showing that local two-point correlation functions equilibrate to a generalized Gibbs ensemble [46,47]. An interesting question is then as follows: What signatures of generalized thermalization appear in an OTOC? We address how our results contribute to this discussion in the Conclusion.

There are therefore many aspects that make the OTOC an object of considerable current interest, and exact numerical results are of significant interest in particular in the presence of disorder. Previous studies [14,18] have in particular focused on MBL systems where both disorder and interactions play an important role and severely limit the sizes that can be reached in numerical calculations. If interactions are neglected, the Jordan-Wigner transformation can be used to study OTOCs. In the absence of disorder, such studies have been performed on the quantum Ising chain [48], quadratic fermions [49], and hard-core boson models [50]. In [48] scrambling was observed at the critical point of the quantum Ising model in the OTOC for operators nonlocal in the Jordan-Wigner fermions.

Here, we turn the attention to the one-dimensional XX spin chain with a random field (RFXX):

$$\hat{H} = J\sum_{i=0}^{L-2}\left(S_i^x S_{i+1}^x + S_i^y S_{i+1}^y\right) + \sum_{i=0}^{L-1}\lambda_i S_i^z, \tag{3}$$

where S_i^x, S_i^y, and S_i^z are the spin-$\frac{1}{2}$ operators at site i, L is the number of sites, J is the interaction coefficient, and the λ_i are the onsite fields applied to the z axis. The λ_i are taken uniformly from the interval $\lambda_i \in [-\lambda, \lambda]$ and we set $\hbar = 1$. We shall refer to λ as the disorder parameter and we shall mainly be concerned with the weak disorder regime $\lambda < J$. This model describes a typical Anderson insulator and is in the AL phase for any nonzero λ. This model is known to be dynamically localized [51] in the sense that it satisfies a zero-velocity Lieb-Robinson bound. Furthermore, entanglement is bounded at all times for this model [38]. However, relatively little is known about the early-time behavior in the model which is the focus of this paper. As we detail below, the Jordan-Wigner transformation is applicable to the random-field XX spin chain also in the presence of disorder and sizable systems can be treated. To simplify the calculation, we exclusively consider open boundary conditions (OBC). We focus on two different scenarios: a quench from a simple Néel-type product state with no entanglement of the following form:

$$|\psi\rangle = \prod_{l\in\mathbb{S}} \hat{S}_l^+ |\downarrow\rangle, \tag{4}$$

where $\mathbb{S} = \{l \in \mathbb{N} : l \mod 2 = 0\}$. The second scenario corresponds to a typical thermal state

$$\rho = \frac{e^{-\beta\hat{H}}}{Z} \tag{5}$$

with $\beta = 1$ and $Z = \mathrm{tr}\,\exp(-\beta\hat{H})$. Expectation values for the two scenarios are then determined as

$$\langle O\rangle_{\text{Néel}} = \langle\psi|O|\psi\rangle \text{ and } \langle O\rangle_{th} = \mathrm{tr}(\rho O). \tag{6}$$

Our principal findings are the following. The propagation of the OTOCs essentially stops beyond a length ξ_{OTOC} that depends on the strength of the disorder λ. For $|x| > \xi_{\text{OTOC}}$ $C(x,t)$ is essentially a constant, $C(x,t)$ in agreement with previous studies [14] performed at strong disorder and very small ξ_{OTOC}. However, for $|x| < \xi_{\text{OTOC}}$ the OTOC propagates information with the *maximal* group velocity $v_{\max} = J$ in the thermodynamic limit. This is the case for both the product and thermal state. For modest λ, ξ_{OTOC} can be sizable. For $|x| < \xi_{\text{OTOC}}$, the early-time regime of $C(x,t)$ is shown to behave as $t^{2|x|}$ in accordance with a recent proposal [48], even in the presence of disorder, $\lambda \neq 0$. For $\lambda \neq 0$, the light cone therefore has the shape of a necktie with a v-shaped tip. While the bipartite entanglement in the RFXX model is bounded at all times [38] we find that the approach to this bound at small λ is rather slow.

The plan of the paper is as follows. In Sec. II we outline some technical aspects of applying the Jordan-Wigner transformation. Section III presents our results for the OTOCs for the two different scenarios detailed above and in Sec. IV discuss our results for the evolution of the entanglement after a quench from the Néel product state. Finally, in Sec. V we attempt to extract a localization length from the bipartite entanglement entropy.

II. JORDAN-WIGNER TRANSFORMATION

In order to study the model (3), we employ the Jordan-Wigner transformation [52]. Using $S_i^{\pm} = (S_i^x \pm iS_i^y)/2$,

$$S_i^+ = \prod_{j=1}^{i-1}(1-2\hat{f}_j^\dagger\hat{f}_j)\hat{f}_i^\dagger, \quad S_i^- = \prod_{j=1}^{i-1}(1-2\hat{f}_j^\dagger\hat{f}_j)\hat{f}_i,$$
$$S_i^z = \hat{f}_i^\dagger\hat{f}_i - \tfrac{1}{2}, \tag{7}$$

we recover a Hamiltonian

$$\hat{H} = \frac{J}{2}\sum_{i=0}^{L-2}(\hat{f}_i^\dagger\hat{f}_{i+1} + \hat{f}_{i+1}^\dagger\hat{f}_i) + \sum_{j=0}^{L-1}\lambda_j\left(\hat{f}_j^\dagger\hat{f}_j - \frac{1}{2}\right), \tag{8}$$

which is a quasi-free-fermionic Hamiltonian with anticommutation relations $\{\hat{f}_k, \hat{f}_l\} = \{\hat{f}_k^\dagger, \hat{f}_l^\dagger\} = 0$ and $\{\hat{f}_l^\dagger, \hat{f}_k\} = \delta_{l,k}$. We adjust the spectrum to get rid of the constant term and write

$$\hat{H} = \sum_{i,j} M_{i,j}\hat{f}_i^\dagger\hat{f}_j, \tag{9}$$

where M is the effective Hamiltonian with entries $M_{i,i} = \lambda_i$ and $M_{i,j} = \frac{J}{2}$ if $|i-j| = 1$. All other entries are zero. This model can be used to study differences between a thermal phase, with no disorder $\lambda = 0$, and the localized phase with $\lambda \neq 0$. When $\lambda = 0$ and we restrict ourselves to the case of $\langle\hat{N}\rangle = \sum_i^L \langle\hat{f}_i^\dagger\hat{f}_i\rangle = \frac{L}{2}$ a regime where the eigenstates of this model typically look locally identical to the Gibbs state [53,54]. However when $\lambda > 0$ the eigenstates are localized and have exponentially decaying correlations characterized by some localization length [38,55,56].

Since M is real symmetric, for a given field realization we can always diagonalize $M = ADA^T$ where $AA^T = \mathbb{I}$ and D is a diagonal matrix with entries $D_{k,k} = \epsilon_k$. Defining new fermionic operators

$$\hat{d}_k = \sum_j A_{j,k}\hat{f}_j, \tag{10}$$

$$\hat{d}_k^\dagger = \sum_j A_{j,k}\hat{f}_j^\dagger, \tag{11}$$

we can then write the Hamiltonian as

$$\hat{H} = \sum_k \epsilon_k \hat{d}_k^\dagger \hat{d}_k, \tag{12}$$

where the ϵ_k are the eigenmodes. A simple reorganization and applications of Wick's theorem when appropriate allows us to express out-of-time ordered correlators in terms of two-point correlations. More details on evaluating the time evolution of this model are presented in Appendix A.

The problem of locality should be addressed. The Jordan-Wigner transformation does not completely conserve locality, the jth pair of fermionic operators are built from the $1, \ldots j$ site spin operators, making it quasilocal. However, the $\hat{S}_i^z$ spin operators are mapped locally to fermions, so we use these operators in the OTOC. Similarly, for the entanglement entropy we consider subregions $A = \{1, \ldots |A|\}$ which are blocks of spin sites preserved by the transformation. We have not considered OTOCs that are not local in the fermion representation as was considered for the quantum Ising model in Ref. [48].

In the following, we mainly focus on the disorder strength $\lambda = 0, 0.3, 0.8$ and we always fix $J = 1$ and $\hbar = 1$. We exclusively consider open boundary conditions. For the results presented in the following sections, we typically use a system size of $L = 400$ and, unless otherwise noted, 1000 disorder realizations of the Hamiltonian are considered and averaged over. We use a simple average to extract mean values over the disorder, leaving a study of the complete distribution over the disorder for further study. When presenting results for several time slices of $C(x,t)$, each value of $C(x,t)$ is shifted vertically by a value of $0.25t$ for visualization purposes.

III. OUT-OF-TIME ORDERED CORRELATIONS

In this section we investigate the out-of-time ordered correlations of the form

$$C(x,t) = \left\langle \left[\hat{\sigma}_i^z(t), \hat{\sigma}_j^z\right]^\dagger \left[\hat{\sigma}_i^z(t), \hat{\sigma}_j^z\right] \right\rangle, \tag{13}$$

where $x = i - j$ is understood to be the displacement between sites i and j. Since $\hat{\sigma}_i^z$ is unitary, we may write

$$C(x,t) = 2(1 - \mathrm{Re}[F(x,t)]). \tag{14}$$

We note that with this definition of $C(x,t)$ the maximum value it can reach is 2. Here,

$$F(x,t) = \left\langle \hat{\sigma}_i^z(t)\hat{\sigma}_j^z\hat{\sigma}_i^z(t)\hat{\sigma}_j^z \right\rangle. \tag{15}$$

We will fix the position of the time-evolved operator as $i = \frac{L}{2}$. Varying j allows us to observe the operator radius spreading over the lattice. As described above, we consider two scenarios: a product state generated by a set of creation operators where $\mathbb{S} = \{l \in \mathbb{N} : l \mod 2 = 0\}$,

$$|\psi\rangle = \prod_{l\in\mathbb{S}} \hat{S}_l^+ |\downarrow\rangle = \prod_{l\in\mathbb{S}} \hat{f}_l^\dagger |0\rangle, \tag{16}$$

where $|\downarrow\rangle$ and $|0\rangle$ are the all spin down and the vacuum state, respectively. This state is a classical Néel state which has the advantage of yielding essentially symmetric initial conditions for spins surrounding the middle lattice point $i = \frac{L}{2}$, allowing us to restrict our studies to one directional displacement on the lattice and having initial fermions distributed evenly in real space. For the second scenario of a thermal state, we construct the Gibbs state with an inverse temperature $\beta = 1$. More details on how these initial conditions are handled and how $C(x,t)$ is calculated can be found in Appendix B.

Before a more detailed discussion of our results for the two different scenarios, we discuss general features of the results for the OTOC and compare the two scenarios in Fig. 1 (solid lines represent results for the product state, dashed lines for the thermal state). Here, Fig. 1(a) show results $C(x, t = 64)$ at a fixed time $t = 64$ versus x. For both the thermal and product states the effects of the disorder are immediately noticeable in the smoothening of $C(x,t)$ that is characteristically oscillating with x in the absence of disorder. For $\lambda \neq 0$, $C(x,t)$ is sharply peaked around $x = 0$ and a clear signature of a wave front where $C(x,t)$ first becomes nonzero is starting to disappear for $\lambda = 0.8$ for this time slice. Figure 1(b) show results for $C(x = 7, t)$ at a fixed separation $x = 7$ versus time. Clear differences between the results for the thermal state and the product state are visible. Most notably, additional structures appear in the peaks of $C(x = 7, t)$ for the product state while the thermal state yields a much smoother oscillation. The long-time behavior of $C(x = 7, t)$ is shown in Fig. 1(c). While $C(x = 7, t)$ clearly goes to zero for $\lambda = 0$ for both scenarios, indicating absence of scrambling, it appears plausible that it attains a finite value in the long-time limit for $\lambda = 0.3, 0.8$ for both scenarios. Since $C(x = 7, t)$ does not saturate for $x = 7$ one could consider this weak (partial) scrambling for $\lambda = 0.3, 0.8$. We note that there is a rather large variation in $C(x = x_0, t)$ with x_0 and as we discuss below $C(|x| > \xi_{\mathrm{OTOC}}, t)$ is essentially zero for *all* t when $\lambda \neq 0$ indicating the absence of scrambling beyond this length scale.

We now turn to a more specific discussion of our results for the Néel product state and thermal state.

A. Product states

In Fig. 2 we show different time slices of $C(x,t)$ versus x. This shell-like structure is expected and parallels the results seen in Ref. [48] for the quantum Ising chain when constructing the OTOC with two operators which are local in the fermionic representation. However, key differences emerge when disorder is introduced by increasing λ. When $\lambda = 0$, we are in a thermal phase and we observe operator spreading over the lattice in the sense that $C(x,t)$ eventually becomes becomes nonzero for any x for large enough t. The operator spreads over the lattice at the maximal group velocity $v_{\max} = J$ as expected. For an individual x, the $C(x,t)$ grows initially in time, peaks, and returns to zero with some rebounding with weaker peaks [see Figs. 1(b) and 1(c)]. Thus, $\lambda = 0$ does not

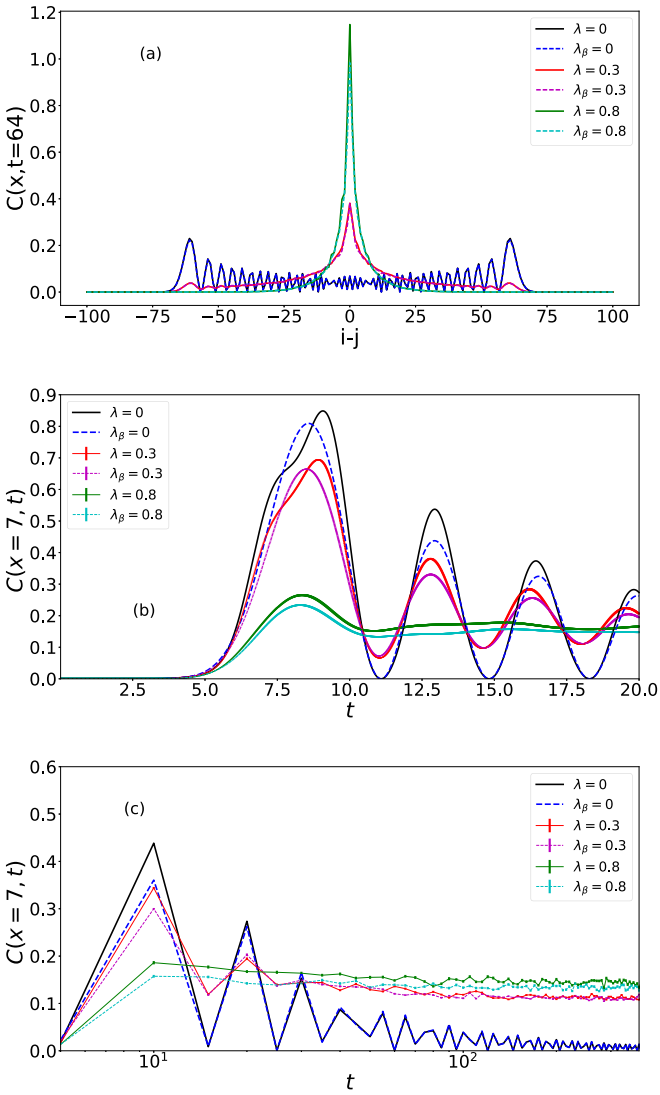

FIG. 1. Results for $C(x,t)$ for three different disorder strengths $\lambda = 0, 0.3, 0.8$. Comparing the product state and thermal state. The labeling λ_β refers to $C(x,t)$ calculated in the thermal state with the specified disorder strength. Solid lines are results for the product state, dashed lines refer to the thermal state at $\beta = 1$. (a) $C(x, t = 64)$ versus x for a fixed $t = 64$, shown as green line in Figs. 2 and 5. (b) Early-time behavior of $C(x = 7, t)$ at $x = 7$, shown as the solid red line in Figs. 2 and 5. (c) Late-time behavior of $C(x = 7, t)$.

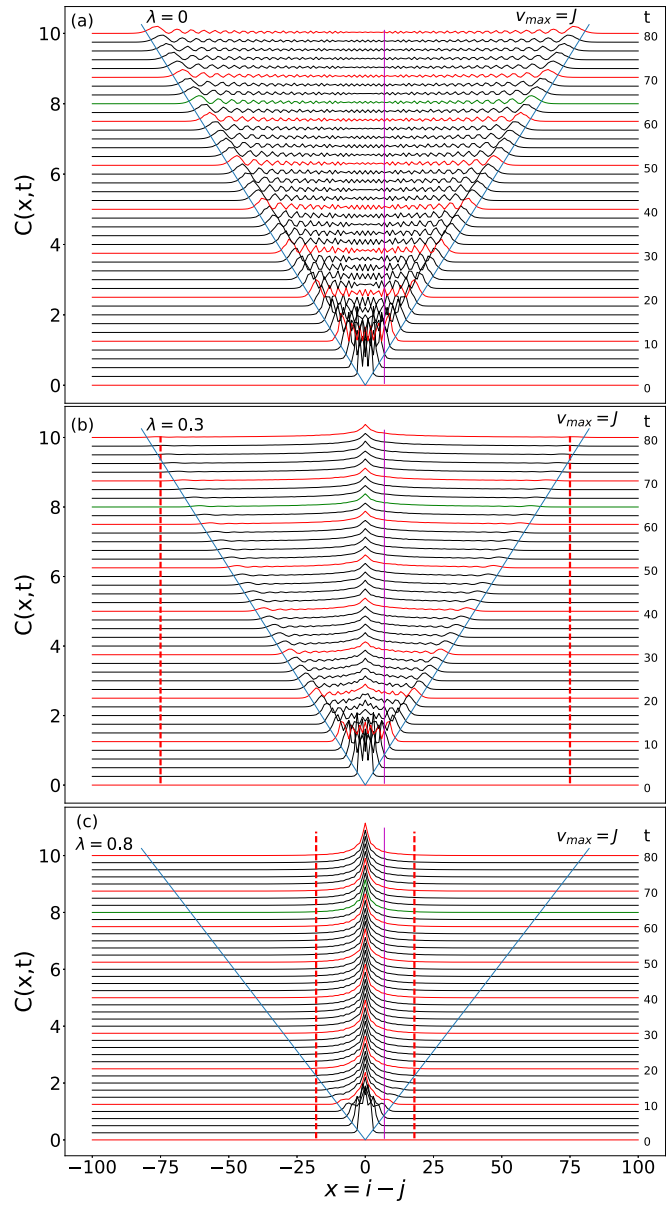

FIG. 2. Wave propagation plot of $C(x,t)$ for the XX spin model at disorder strength (a) $\lambda = 0$, (b) $\lambda = 0.3$, and (c) $\lambda = 0.8$. For visualization, each value of $C(x,t)$ is shifted vertically by a value of $0.25t$, demonstrating the operators radius spreading. The x axis is the displacement from the center of the chain $i = \frac{L}{2}$. The two y axes are the values $C(x,t)$ and the corresponding time. The maximal group velocity $v_{\max} = J$ is also shown (solid blue line). In (b) and (c), the vertical dashed red line indicates ξ_{OTOC}, the x value beyond which $C(x,t) < 10^{-3}$ for any x. $\xi_{\text{OTOC}} = 18$ for $\lambda = 0.8$ and 75 for $\lambda = 0.3$.

scramble. For $\lambda = 0.3$ and 0.8 we observe operator spreading at the *maximal* group velocity for $|x| < \xi_{\text{OTOC}}$ [where ξ_{OTOC} characterizes a length sufficiently large compared to the localization length such that the commutation relation bound is sufficiently small as seen in Eq. (17)]. However, for values of $|x| > \xi_{\text{OTOC}}$, $C(x,t) = 0$ for all times. ξ_{OTOC} is shown in Figs. 2(b) and 2(c) as the dashed vertical red lines and indicated the length scale beyond which $C(x,t) < 10^{-3}$ for all times. Hence, the operator radius is bounded by ξ_{OTOC} and does not spread into regions beyond ξ_{OTOC}. As expected, ξ_{OTOC} shrinks with increasing λ, as seen in Figs. 2(b) and 2(c). For $|x| < \xi_{\text{OTOC}}$, $C(x,t)$ initially grows with t until it peaks and then decreases to weakly oscillate around a nonzero value, and never returns to zero. This is a fundamentally different behavior than the no-disorder case. This long-time limit of $C(x,t)$ for $|x| < \xi_{\text{OTOC}}$ increases weakly with λ while it decreases with x. The light cone has therefore the shape of a necktie with a v-shaped tip. This behavior is markedly different from results in MBL systems where a much different logarithmic light cone has been observed [15,18,21].

In Refs. [12,51] it has been noted that the Anderson localized states do exhibit a nonexpanding light cone with the

commutator between two operators being bounded in time by

$$|||[A(0,0),B(x,t)]||| \leqslant Ce^{-\frac{|x|}{\xi}}, \tag{17}$$

where $A(0,0)$ and $B(x,t)$ are operators with local support and x is the displacement in-between them. This result implies that $C(x,t)$ should have the same exponential behavior and we have verified that the results in Fig. 1(a) for $\lambda = 0.8$ and for $|x| < 8$ are well described by

$$C(x, t = 64) \sim e^{-a|x|}, \tag{18}$$

with $a \sim 0.33$. In Ref. [48] it was proposed that a universal power law applies to all lattice systems where the Hamiltonian is constructed from local interactions. For the quantum Ising model this was shown to be [48] $C(x,t) \sim t^{2(2x-1)}$. This is seen by considering the Hadamard formula, and an operator $\hat{A}$ (see Ref. [57], Lemma 5.3):

$$e^{s\hat{H}}\hat{A}e^{-s\hat{H}} = \hat{A} + s[\hat{H},\hat{A}] + \frac{s^2}{2!}[\hat{H},[\hat{H},\hat{A}]]\cdots = \sum_{n=0}^{\infty}\frac{s^n}{n!}L_n. \tag{19}$$

For the RFXX spin chain considered here we arrive at a slightly modified power law by repeating the argument of Ref. [48]. This is done by considering $\hat{A} = \hat{\sigma}^z_{\frac{L}{2}}$ and $s = it$ and determining the smallest n of the above sum, such that $[L_n, \sigma^z_{j=x}] \neq 0$. This corresponds to successively evaluating the commutator between the Hamiltonian and the string of operators that grows until it reaches $j = x$. The strings which appear at the smallest order of t for odd n look like (shifting the indexes for simplicity) $\hat{\sigma}^x_0\hat{\sigma}^z_1\hat{\sigma}^z_2\ldots\hat{\sigma}^z_{x-1}\hat{\sigma}^y_x$ and $\hat{\sigma}^y_0\hat{\sigma}^z_1\hat{\sigma}^z_2\ldots\hat{\sigma}^z_{x-1}\hat{\sigma}^x_{j=x}$, while for n even, $\hat{\sigma}^x_0\hat{\sigma}^z_1\hat{\sigma}^z_2\ldots\hat{\sigma}^z_{x-1}\hat{\sigma}^x_x$ and $\hat{\sigma}^y_0\hat{\sigma}^z_1\hat{\sigma}^z_2\ldots\hat{\sigma}^z_{x-1}\hat{\sigma}^y_{j=x}$, yielding $n = j = x$. At least for regions inside the light cone we expect this behavior to be independent of λ. With $C(x,t)$ the square of the commutator, we then find for the RFXX model at early times

$$C(x,t) \sim t^{2|x|}, \tag{20}$$

with a power law that is independent of λ and is therefore *not* modified by the presence of disorder. This is purely a quantum mechanical phenomenon occurring before the wave front hits and is not a signature of scrambling. This phenomenon is captured in Fig. 3 where results are shown for $\lambda = 0$ [Fig. 3(a)], $\lambda = 0.3$ [Fig. 3(b)], and $\lambda = 0.8$ [Fig. 3(c)] where results are shown for a range of values of x confirming the above power-law dependence. For $|x| = 2, 4$ we include the next leading term in the fits: $t^{2(|x|+1)}$. The power-law growth in this model is thus universal for $\lambda = 0$ as well as in the the localized phase ($\lambda \neq 0$), assuming we are inside the light cone. Interestingly, outside of the light cone, despite the derivation for the power law being independent of λ, the power law breaks down, signifying localization suppressing quantum effects as well. Precisely, how localization effects will start to dominate is not clear, although the clear presence of correction terms for $|x| < \xi_{\mathrm{OTOC}}$ is an indication that such corrections eventually become dominant.

Finally, we study the behavior of $C(x,t)$ at the wave front which moves at a velocity $v_{\max} = J = 1$. Here, we use (following Ref. [48]) the function

$$G(x,t) = \frac{\partial \ln C(x,t)}{\partial t} = \frac{1}{C(x,t)}\frac{\partial C(x,t)}{\partial t}. \tag{21}$$

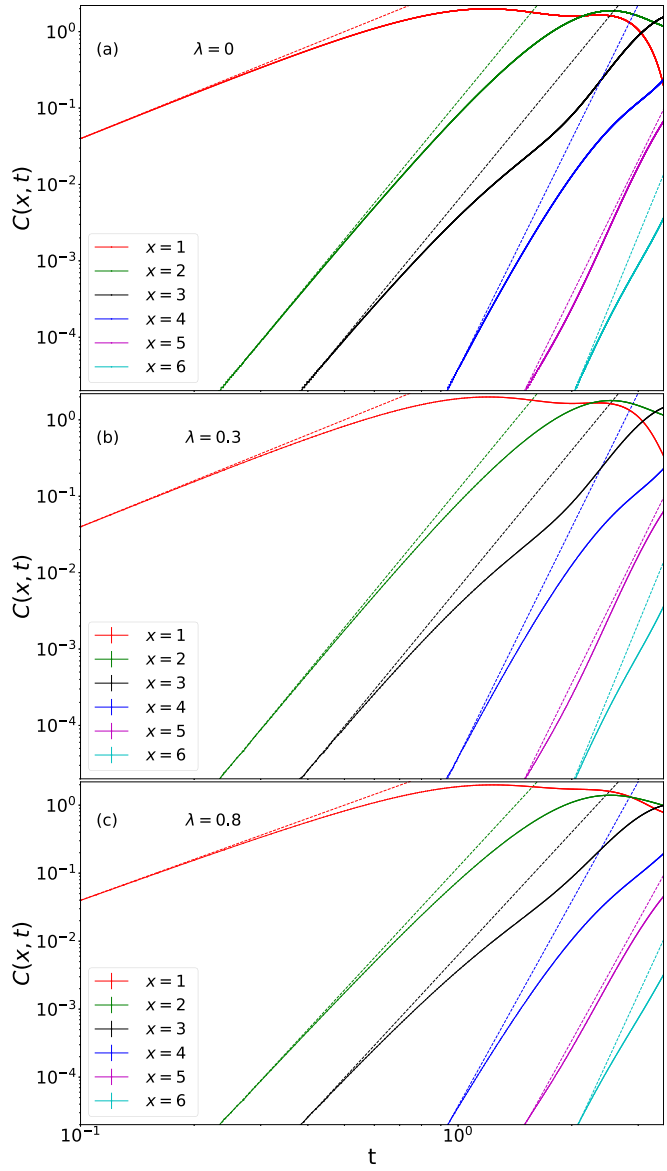

FIG. 3. Early time $C(x,t)$ at different values of x for each studied λ. The dotted lines for $x = 1, 3, 5, 6$ are the power laws $t^{2|x|}$ with appropriate constants in front while the solid lines are the actual data. For $x = 2, 4$ the next leading order power $t^{2(|x|+1)}$ is required to fit the data for every value of λ.

Since we know the expression for $C(x,t)$ exactly $G(x,t)$ can be calculated without resorting to evaluating the derivatives numerically. Our results for this function are plotted in Fig. 4. The wave front hits when $t - \frac{x}{J} = 0$, and we again see the initial purely quantum mechanical growth of $C(x,t)$ before the front hits. After the wave front hits $G(x,t)$ in all cases becomes negative after a short time, and then an oscillatory behavior about 0 is observed. For $\lambda = 0$, the repeating pattern appears to have a discontinuous change when going from negative to positive values of $G(x,t)$, however, this is most likely an artifact of $C(x,t)$ returning to zero and bouncing back upward as seen in Fig. 2. Because this behavior is observed for extremely large values of t and large accessible system sizes, we cannot conclude exactly how $C(x,t)$ goes

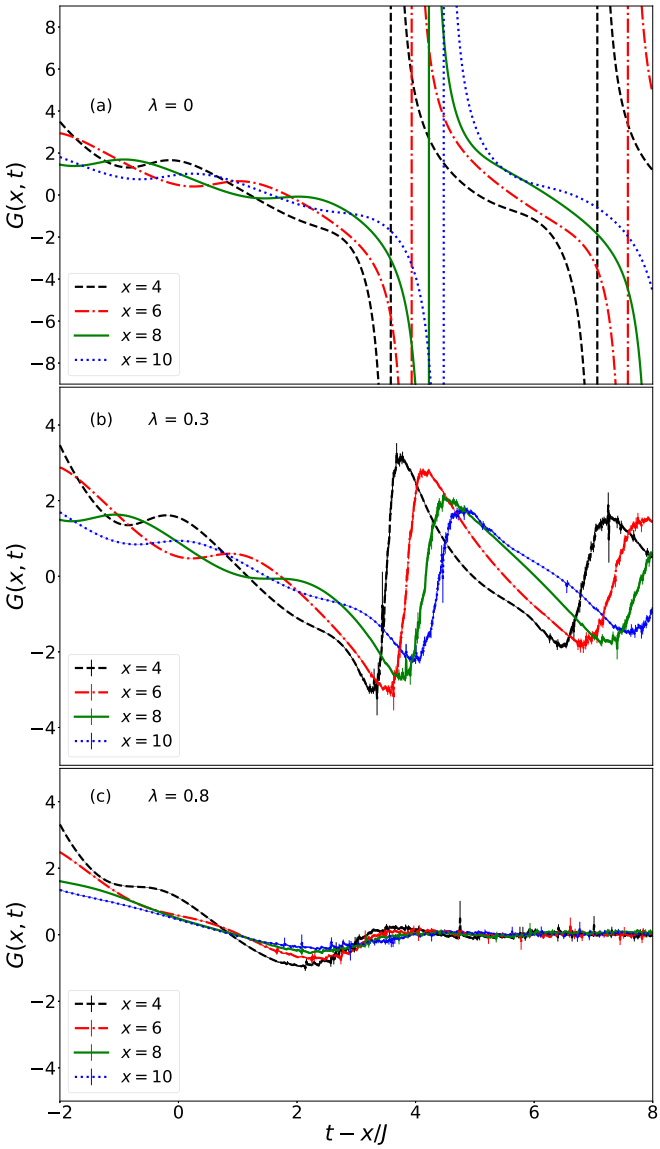

FIG. 4. $G(x,t)$ graphed against $t - \frac{x}{t}$. This simulation required 5000 realizations of the random Hamiltonian to get reasonable error bars. All averages were taken over the function $G(x,t)$ itself.

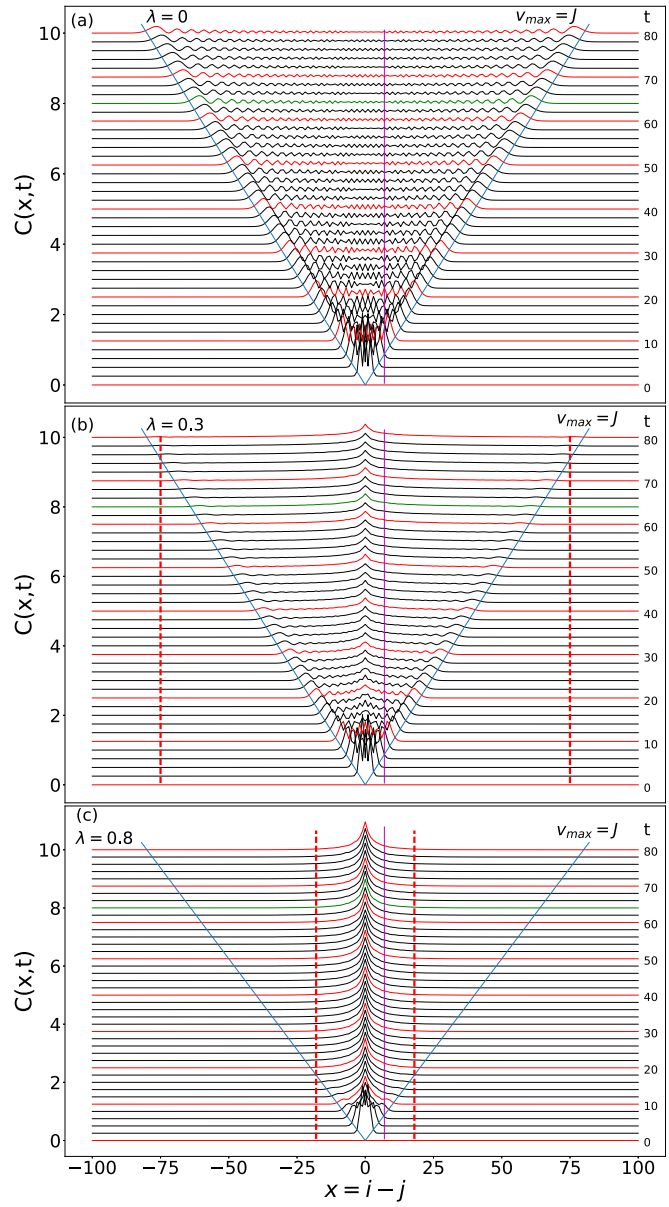

FIG. 5. Wave propagation plot of $C(x,t)$ for the RFXX spin chain at disorder strength (a) $\lambda = 0$, (b) $\lambda = 0.3$, and (c) $\lambda = 0.8$ in a thermal state with $\beta = 1$. The x axis is the displacement from the center of the chain $i = \frac{L}{2}$ symmetry about the position i the wave propagates symmetrically. The two y axes are the values $C(x,t)$ and the corresponding time. The maximal group velocity $v_{\max} = J$ is also shown as the solid blue line. In (b) and (c) the vertical dashed red line indicates ξ_{OTOC}, the x value beyond which $C(x,t) < 10^{-3}$ for any x. $\xi_{\text{OTOC}} = 18$ for $\lambda = 0.8$ and 75 for $\lambda = 0.3$.

to zero as $t \to \infty$ for $\lambda = 0$. For $\lambda \neq 0$ the behavior is different since $C(x,t)$ does not go back to zero, but instead oscillates around a nonzero value. However, we see that as λ is increased, $G(x,t)$ varies much less rapidly. Both $\lambda = 0.3$ and 0.8 show oscillatory behavior in $G(x,t)$ after the wave front reaches but the amplitudes are suppressed with larger λ. Interestingly, we do not observe monotonic behavior on any meaningful interval.

B. Thermal states

Next, we repeat these calculations, but with a thermal state with $\beta = 1$ instead of the product state considered in the previous section. $\beta = 1$ is an arbitrary choice because the dynamics will overall depend primarily on the anticommutator in time (which is β independent), for both disorder and nondisorder. Hence, the variation with β is relatively minor, in particular in the presence of disorder. This state is already in equilibrium and exhibits a significantly different expression for $C(x,t)$ as detailed in Eq. (B8). In Fig. 5 we show $C(x,t)$ at different time slices. Although this plot looks similar to the product state version, Fig. 2, differences emerge. First, the peaks of the $C(x,t)$ are smaller than was the case for the product state, and the $C(x,t)$ is much smoother as seen in Fig. 1, traveling simply as a smooth parabolalike curve in space. However, the oscillatory behavior occurs also in

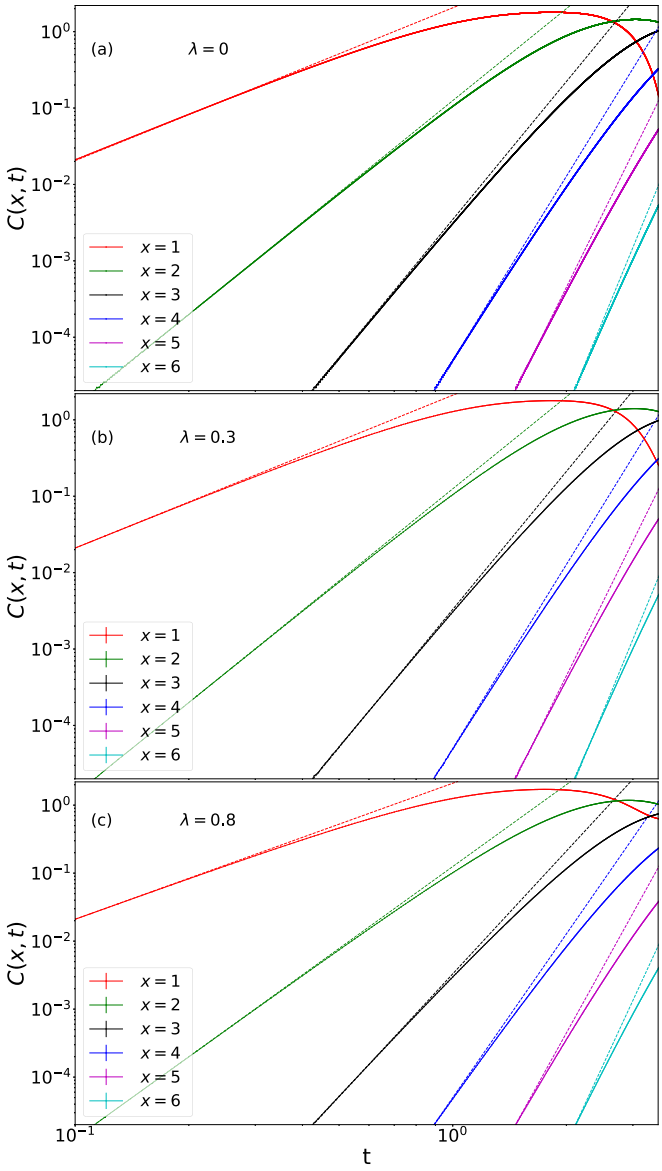

FIG. 6. Early-time $C(x,t)$ thermal correlations at different values of x for $\lambda = 0, 0.3, 0.8$. The dotted lines for $x = 1, 2, 3, 4, 5, 6$ are the power laws $t^{2|x|}$ with appropriate constants in front while the solid lines are the actual data.

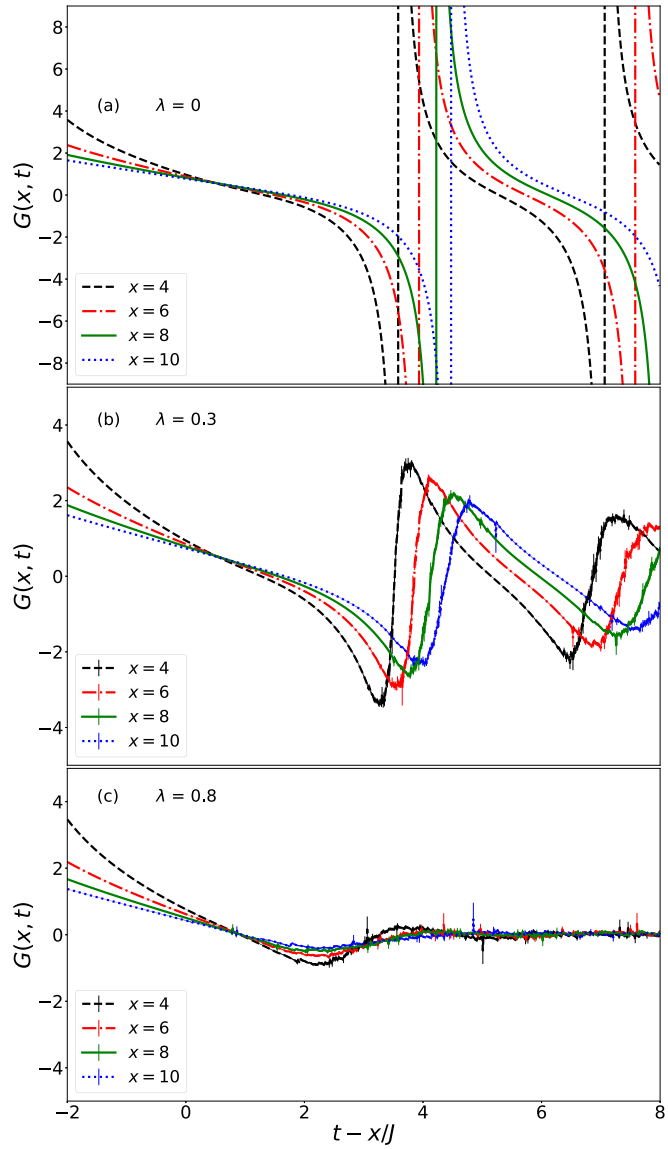

FIG. 7. $G(x,t)$ as a function of $t - \frac{x}{J}$ calculated in the thermal state with $\beta = 1$. This simulation required 5000 realizations of the random Hamiltonian to get reasonable error bars.

this case, and we again do not expect to be able to find a description for how $C(x,t)$ approaches zero in late time. For this value of $\beta = 1$ we find the same values for ξ_{OTOC} as was determined for the Néel product state.

We also see in Fig. 6 that the thermal states obey the power law discussed in Eq. (20). For the thermal state the agreement with the power-law behavior is better than for the product state and no higher-order terms are included in the fits shown in Fig. 6. This is most likely due to the absence of noise, which indicates modeling the wave front will be easier with this initial condition.

Finally, in Fig. 7, we show the wave front as described by $G(x,t)$ evaluated using the thermal state with $\beta = 1$. Unlike the product state we observe monotonic behavior for the approximate region $t - \frac{x}{J} \in [-2, 2]$ and we observe strong x and λ dependence. Once again, the $\lambda = 0$ diverges when $C(x,t)$ goes to zero, and the $\lambda \neq 0$ cases do not exhibit this behavior due to $C(x,t)$ never returning to zero. Similarly, we observe oscillatory behavior after the wave front passes. At the wave front which we define as $t - \frac{x}{J} \in [0, 2]$ we can effectively approximate $G(x,t)$ by a linear equation $G(x,t) \approx m(t - x/J) + c = at + b$, due to the shapes of the functions we expect $a = a(x, \lambda)$ and $b = b(x, \lambda)$. Interestingly, this form suggests that at the wave front

$$C(x,t) \sim e^{\frac{a(x,\lambda)t^2}{2} + b(x,\lambda)t}. \tag{22}$$

To follow the universal form of Eq. (2) one must have

$$G(x,t) \sim \frac{\lambda_L}{t^{p+1}}(x - v_B t)^p (v_B t + px). \tag{23}$$

However, the form of Eq. (23) does not permit a linear equation. Thus, we conclude that our results in Eq. (22) do

TABLE I. Results of fitting the function $G(x,t) \approx m(t - x/J) + c = at + b$ where on the interval $t - \frac{x}{J} \in [0, 2]$ for different values of λ and x. The errors reported are one standard deviation on the parameter.

$\lambda = 0$	m	c
$x = 2$	-0.72948875 ± 0.002	0.94258389 ± 0.002
$x = 4$	-0.59368064 ± 0.001	0.88059725 ± 0.001
$x = 6$	-0.5040499 ± 0.0009	0.82791869 ± 0.001
$x = 10$	-0.44021805 ± 0.0008	0.78445194 ± 0.0009
$\lambda = 0.3$	m	c
$x = 2$	-0.73975833 ± 0.002	0.92284197 ± 0.002
$x = 4$	-0.60431888 ± 0.001	0.85326093 ± 0.001
$x = 6$	-0.51342755 ± 0.001	0.7949133 ± 0.001
$x = 10$	-0.44742463 ± 0.0009	0.74793077 ± 0.001
$\lambda = 0.8$	m	c
$x = 2$	-0.81713901 ± 0.002	0.74741784 ± 0.003
$x = 4$	-0.63429921 ± 0.002	0.60081936 ± 0.003
$x = 6$	-0.52336579 ± 0.003	0.4942889 ± 0.003
$x = 10$	-0.40722873 ± 0.003	0.40339502 ± 0.004

not follow the proposed universal form (2). We currently do not know an exact expression for $a(x, \lambda)$ and $b(x, \lambda)$, however, for completeness we provide a table of the fitted values in Table I. The values for $a = m$ are necessarily negative and c positive. The errors reported are one standard derivation. The small errors indicate that the form given in Eq. (22) is a reasonable description.

IV. BIPARTITE ENTANGLEMENT ENTROPY

We now turn to a discussion of the growth of entanglement in the RFXX starting from the Néel product state which, due to its product form, has zero entanglement. The entanglement entropy between two subsystems A, B is defined with the reduced density matrices $\rho_A = \mathrm{tr}_B \rho$ and $\rho_B = \mathrm{tr}_A \rho$,

$$S_{A,B} = -\mathrm{tr}(\rho_A \ln \rho_A) = -\mathrm{tr}(\rho_B \ln \rho_B), \tag{24}$$

where the equality is taken because regardless of the partition ρ_A and ρ_B have identical nonzero eigenvalues [58]. For the remainder of this section we partition the lattice into halves and denote this quantity as $S_{\frac{L}{2}}$.

Rigorous bounds for the entanglement entropy in the RFXX model in the Anderson localized phase have been derived and it is expected to obey an area law in one dimension [38,55,59]. In particular, it has been shown that the growth of entanglement remains bounded for all times [38]. This means entanglement entropy even for arbitrarily small disorder strengths will be bounded by a constant in the late-time limit. The approach to this limiting value is relatively less explored and that is our focus here. Exact diagonalization results on small systems have been discussed in Ref. [34] where for relatively strong disorder the entanglement entropy reached a constant at very short times.

In order to study the time-dependent entanglement, we time evolve our state, Eq. (16), and calculate the entanglement entropy at late times. We expect that at sufficiently large system sizes we will not observe an increase in entanglement entropy as the system grows since we will be

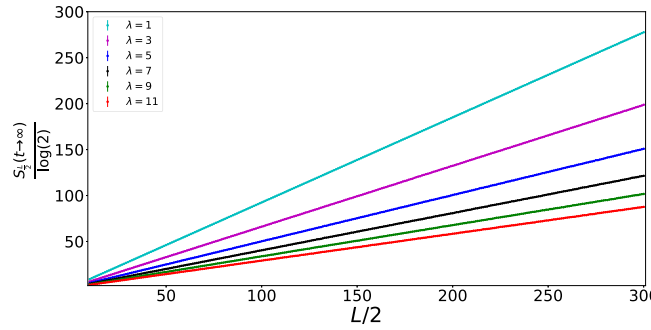

FIG. 8. Infinite-time average $S_{\frac{L}{2}}$ plotted against system size. Each point is an average over 5000 random-field realizations and the error shown is the standard error on the calculated mean. System sizes are taken from $L = 20$ to 600. For these results the approximation yielding the infinite-time average is *not* valid and the resulting volume law is *incorrect*.

close to the theoretical maximum. In Ref. [34] the authors did a similar calculation for both Anderson and many-body localized phases. However, comparing many-body localized systems to Anderson localized systems restricts the system sizes; here we do not have this restriction, focusing entirely on the Anderson localization regime. Using the method in [60] we can efficiently calculate the entanglement entropy from the occupation matrix defined in Eq. (A12). Since we are interested in late-time entanglement entropy, it is tempting to consider the infinite-time average of the occupation matrix. That is, for each element, we define (similar to [61])

$$\begin{aligned}\Lambda^f(\infty)_{i,j} &:= \lim_{T\to\infty} \int_0^T dt \frac{1}{T} \langle \hat{f}_i^\dagger(t) \hat{f}_j(t) \rangle \\ &= \lim_{T\to\infty} \int_0^T dt \frac{1}{T} \sum_{k,l} e^{i(\epsilon_k - \epsilon_l)t} A_{i,k} A_{j,l} \langle \hat{d}_k^\dagger \hat{d}_l \rangle \\ &= \sum_k A_{i,k} A_{j,k} \langle \hat{d}_k^\dagger \hat{d}_k \rangle, \end{aligned} \tag{25}$$

which amounts to a "dephasing" of the off-diagonal contributions. Note that we used the fact that the ϵ_k are expected to be nondegenerate [56]. The infinite-time average occupation matrix corresponds to a generalized Gibbs ensemble

$$\rho = \frac{1}{Z} e^{-\sum_k \beta_k \hat{Q}_k}, \tag{26}$$

where $\hat{Q}_k = \hat{d}_k^\dagger \hat{d}_k$.

However in Fig. 8 we see that the infinite-time average occupation matrix predicts volume laws despite large disorder; the disorder only changes the slope, but the entanglement entropy still grows linearly with system size. This is most likely due to the infinite-time average being a valid approximation for the equilibrated occupation matrix *only on small subsystems*, where the difference disappears with the system size. However, here we are focusing on subsystems which are a constant fraction of the system we are growing. Thus, the errors that disappear on a small scale add up on the macroscopic scale and we lose the ability to effectively describe the equilibrated state with the infinite-time average. The above approximation is therefore *not valid* in the present

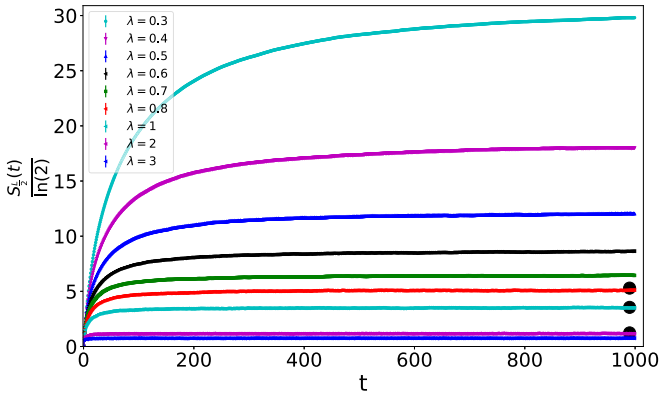

FIG. 9. $S_{\frac{L}{2}}$ plotted against time for a system size of $L = 400$. Results are shown for $\lambda = 0.3, 0.4, 0.5, 0.6, 0.7, 0.8, 1, 2, 3$. Each point is an average over 1000 field realizations and the error shown is the standard error on the calculated mean. The black dots pictured are the maximum values observed for times up to $t = 10^8$ for $\lambda = 0.8, 1, 2$.

case. Instead, we must pick an arbitrary late time to calculate the entanglement entropy which we here take to be $t = 10^{11}$.

In Fig. 9 we show results for the growth of the average entanglement entropy with time for the range of disorders we are interested in. It has been proposed that the saturation time for entanglement entropy $\log(t_{\text{sat}}) \sim L$ [34]. Intuitively, for the Anderson insulator, taking a localization value $\xi(\lambda) \ll L$ we would expect the time it takes for the entanglement entropy to get close to this saturated value to be much smaller, as only small subsystems become entangled with each other. This is indeed what we see in Fig. 9, by $t = 500$ all but $\lambda = 0.3$ have little to no growth, and $\lambda = 0.3$ has slowed significantly compared to its initial rise. However, the approach to a constant value could involve logarithmic factors and for subsequent analysis we therefore chose to study the entanglement at $t = 10^{11}$. Three black dots are also included to indicate the maximum value observed at $t = 10^8$. The three dots show the entanglement entropy at the disorder strengths $\lambda = 0.8, 1, 2$. It was recently reported that other localized systems which can be mapped to free fermions show $\log t$ growth at late times [42]. The authors observed this intriguing behavior beginning at around $t = 10^6$ and we confirm here this is *not* observed in the Anderson insulator up to the times considered. The entanglement entropy behavior only marginally changes from $t = 10^3$ to 10^8.

In Fig. 10 we show results for the entanglement entropy versus $L/2$ at $t = 10^{11}$ as we vary the system size. We observe that as the system size is increased, the slope of $S_{\frac{L}{2}}(t \to \infty)$ is not constant. Instead, $S_{\frac{L}{2}}(t \to \infty)$ is indeed approaching a constant value as we increase system size. This means the system is approaching an area law as the system size significantly exceeds the localization length consistent with other studies [38,55]. However, as is particularly evident for $\lambda = 0.3$, there can be an extended range of system sizes for which S is linear in $\log(L)$.

V. LOCALIZATION LENGTH

In this section we use the data from Fig. 10 to define a quantity ξ which is a measure of the localization length

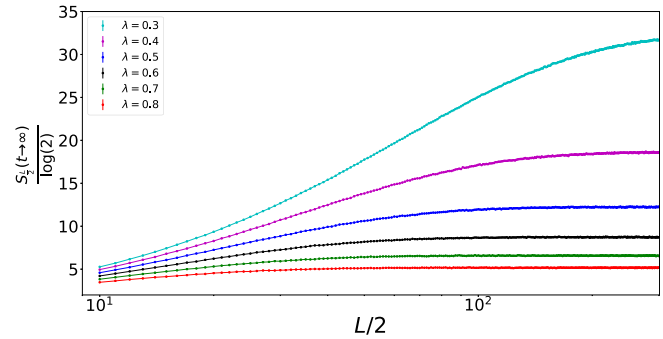

FIG. 10. $S_{\frac{L}{2}}$ plotted against system size at $t = 10^{11}$. Each point is an average over 5000 random-field realizations and the error shown is the standard error on the calculated mean. System sizes are taken from $L = 20$ to 600. Note the logarithmic x axis.

in the RFXX. We say the system is completely localized when the entanglement entropy between our two subsystems does not grow as we increase the system. When L is small, unless disorder is extremely large, we expect the entanglement entropy to grow sublinearly in L but it will still grow. So, by adding one site to each subsystem, we grow the lattice and determine the slope of $S_{\frac{L}{2}}$ with $L/2$. We can then define the rate of growth:

$$m(L/2) := S_{\frac{L}{2}} - S_{\frac{L}{2}-1}. \tag{27}$$

In the localized regime we expect that

$$\lim_{L\to\infty} m(L/2) = 0. \tag{28}$$

The data, however, are not strictly increasing due to noise, so to improve the fitting we use a Savitzky-Golay filter to smooth the data and compute $m(L/2)$ with the smoothed version of the data. Defining a tolerance ϵ, such that $m(L/2) < \epsilon$, we can then define $\xi(\lambda) = \frac{L}{2}$ by the first L for which this occurs. We choose ϵ to be reasonably small since it indicates that the function $m(L/2)$ is approaching the area law. Our results are shown in Fig. 11 clearly indicating a diverging ξ as $\lambda \to 0$. The fitted function takes the form $a\sqrt{x} + b$ with standard deviations on the variables smaller than 3×10^{-3}. The value of b was found to be $b = -0.008\,663\,31$ and we expect this value to approach zero as values closer to $\lambda = 0$ are probed. It

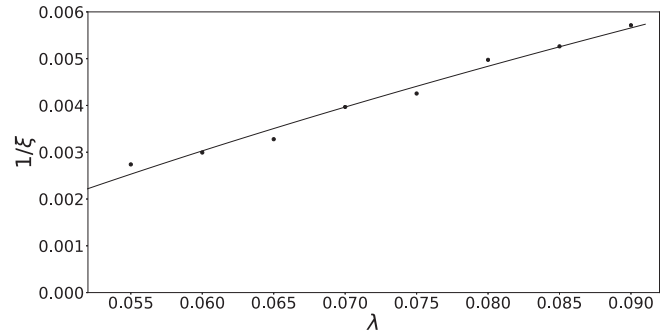

FIG. 11. $\frac{1}{\xi}$ plotted against λ. The data from $S_{\frac{L}{2}}$ were smoothed out using a Savitzky-Golay filter with a polynomial of degree 2 and a window of 11, and a tolerance $\epsilon = 0.37$. Each value of $S_{\frac{L}{2}}$ was computed with over 20 000 realizations of the Hamiltonian.

is at present not clear how reliable the above analysis is for a precise determination of the critical exponents, but the results strongly suggest a diverging length scale as $\lambda \to 0$.

VI. CONCLUSION

The presence of disorder in the RFXX has been shown to significantly alter the behavior of the OTOCs. At a finite disorder-dependent ξ_{OTOC} information propagation stops and the OTOCs are essentially zero beyond this length scale. However, for $|x| < \xi_{\mathrm{OTOC}}$ we find propagation at the maximal speed $v = J$ and confirm a power-law behavior for the early-time regime of $C(x,t) \sim t^{2x}$ with a position-dependent exponent. An analysis of the behavior of $C(x,t)$ close to the wave front shows a behavior that is not consistent with recent predictions. The growth of the entanglement starting from an unentangled product state shows saturation at sufficiently large times. We have not been able to isolate any specific temperature-dependent effects and, in the light of a temperature-dependent maximal bound on the Lyaponov exponents $\lambda_L \leqslant 2\pi k_B T/\hbar$, further studies would be of interest.

Finally, our results shed some light on the connection between thermalization and scrambling. We observed *weak* scrambling in the localized phase ($\lambda \neq 0$) of the RFXX. From the results of Ref. [62] it is known that relaxation in a closely related model is described by a generalized Gibbs ensemble with an *extensive* number of conserved quantities. We also observe an absence of scrambling in the nondisordered ($\lambda = 0$) case which requires an *intensive* number of conserved quantities in the corresponding generalized Gibbs ensemble [47]. Hence, the absence of scrambling does not imply the absence of a generalized form of thermalization and a sign of "weak" scrambling does not imply thermalization in the traditional sense.

ACKNOWLEDGMENTS

This research was supported by NSERC and enabled in part by support provided by (SHARCNET) (www.sharcnet.ca) and Compute/Calcul Canada (www.computecanada.ca).

APPENDIX A: TIME-EVOLVING FREE FERMIONS

In this Appendix we review how to time evolve free fermions. A similar treatment can be found in [61]. Starting from the Hamiltonian

$$\hat{H} = \sum_{i,j} M_{i,j} \hat{f}_i^\dagger \hat{f}_j, \tag{A1}$$

where M is a real $L \times L$ symmetric matrix and for generality we do not make any other assumption. This model represents a one-dimensional system of quasi-free fermions hopping on a lattice. The fermionic operators $\hat{f}_i^\dagger$ and $\hat{f}_i$ obey the anticommutation relations

$$\{\hat{f}_j^\dagger, \hat{f}_k\} = \delta_{jk}, \quad \{\hat{f}_j^\dagger, \hat{f}_k^\dagger\} = \{\hat{f}_j, \hat{f}_k\} = 0. \tag{A2}$$

Since M is real symmetric we can always diagonalize it as $M = ADA^T$ where $AA^T = \mathbb{I}$ is real orthogonal transformation and D is a diagonal matrix with entries $D_{k,k} = \epsilon_k$ which are (real) energy eigenmodes. Defining new fermion operators

$$\hat{d}_k = \sum_j A_{j,k} \hat{f}_j, \tag{A3}$$

$$\hat{d}_k^\dagger = \sum_j A_{j,k} \hat{f}_j^\dagger, \tag{A4}$$

we can write the Hamiltonian as

$$\hat{H} = \sum_k \epsilon_k \hat{d}_k^\dagger \hat{d}_k. \tag{A5}$$

The above operators can be referred to as reciprocal space or normal mode operators. These operators inherit fermionic anticommutation relations due to the unitary property of A:

$$\{\hat{d}_l, \hat{d}_k^\dagger\} = \sum_{i,j} A_{i,l} A_{j,k} \{\hat{f}_i, \hat{f}_j^\dagger\} = \delta_{l,k}. \tag{A6}$$

Due to the definition of the annihilation operators, it is easy to see that $|0\rangle_f = |0\rangle_d$. Thus, all eigenstates can be constructed by applying creation operators $\hat{d}_k^\dagger$. These states are Gaussian, meaning they are completely described by their second moments. Gaussian states can be completely described by the occupation matrix $\Lambda^f_{i,j} = \langle \hat{f}_i^\dagger \hat{f}_j \rangle$ or, in eigenmode space, $\Lambda^d_{l,k} = \langle \hat{d}_l^\dagger \hat{d}_k \rangle$. All time-evolved properties of this model can similarly be deduced by time evolving the occupation matrix. It is simple to time evolve the operators in eigenmode space,

$$\frac{d}{dt}(\hat{d}_k) = i[\hat{H}, \hat{d}_k], \tag{A7}$$

where

$$\hat{H} = \sum_k \epsilon_k \hat{d}_k^\dagger \hat{d}_k. \tag{A8}$$

Using $\{\hat{d}_k, \hat{d}_l^\dagger\} = \delta_{l,k}$ and $\hat{d}_k^2 = 0$, one finds that

$$\hat{d}_k(t) = e^{-i\epsilon_k t} \hat{d}_k, \tag{A9}$$

similarly for the creation operators

$$\hat{d}_k(t)^\dagger = e^{i\epsilon_k t} \hat{d}_k^\dagger; \tag{A10}$$

this then implies

$$\Lambda^d(t) = e^{iDt} \Lambda^d e^{-iDt}, \tag{A11}$$

which means if we know $\Lambda^d(0) = \Lambda^d$ we can compute $\Lambda^d(t)$, giving us all two-point correlators taken at identical times. Because we want to extract local statistics, we need to transform back to the local fermion space. We see this is done by the following transformation:

$$\Lambda^f(t) = A e^{iDt} \Lambda^d e^{-iDt} A^T, \tag{A12}$$

where $\Lambda^d = A^T \Lambda^f A$. Now, since we will also be interested in out-of-time correlations, it becomes important to consider two-point correlations which are taken at different times. For this we introduce the following notation $\Lambda^f(t,t)$, where the left t argument indicates that the creation operators $\hat{d}_k^\dagger$ are at a time t and the right for the annihilation operators. Thus,

Eq. (A12) is $\Lambda^f(t) = \Lambda^f(t,t)$ and the out-of-time two-point correlators are given by

$$\Lambda^f(t,t) = Ae^{iDt}\Lambda^d e^{-iDt}A^T, \tag{A13}$$

$$\Lambda^f(t,0) = Ae^{iDt}\Lambda^d A^T, \tag{A14}$$

$$\Lambda^f(0,t) = A\Lambda^d e^{-iDt}A^T. \tag{A15}$$

With Eqs. (A13)–(A15) we can calculate any two-point correlator that might be expressed in the OTOC. Next, it is important to see how the anticommutation rule behaves as we consider creation and annihilation operators at different times. In local space, consider the case where one operator in the Heisenberg picture is taken at $t = 0$ and the other at $t = t$:

$$\{\hat{f}_m^\dagger(t), \hat{f}_n^\dagger\} = \sum_{k,l} A_{n,l}A_{m,k}e^{i\epsilon_k t}(\hat{d}_k^\dagger\hat{d}_l^\dagger + \hat{d}_l^\dagger\hat{d}_k^\dagger) = 0. \tag{A16}$$

Similarly, $\{\hat{f}_m(t), \hat{f}_n\} = 0$, however, the anticommutation between out-of-time creation and annihilation operators is nontrivial:

$$\{\hat{f}_m^\dagger(t), \hat{f}_n\} = \sum_k A_{m,k}A_{n,k}e^{i\epsilon_k t} = a_{m,n}(t). \tag{A17}$$

At $t = 0$ we see $a_{m,n}(0) = \delta_{m,n}$, but time evolution removes this nice behavior. We also see that

$$\bar{a}_{m,n}(t) = \{\hat{f}_m(t), \hat{f}_n^\dagger\} = \sum_k A_{m,k}A_{n,k}e^{-i\epsilon_k t}. \tag{A18}$$

With these tools in place, it is convenient to write the correlations exactly which will be featured in the OTOC. Consider two sites on the lattice labeled by i and j at $t = t$ and 0, respectively, then the time-dependent correlations are taken from entries of Eqs. (A13)–(A15):

$$\Lambda^f(t,t)_{i,i} = \langle\hat{f}_i^\dagger(t)\hat{f}_i(t)\rangle = \sum_{k,l} e^{i(\epsilon_k-\epsilon_l)t}A_{i,k}A_{i,l}\langle\hat{d}_k^\dagger\hat{d}_l\rangle, \tag{A19}$$

$$\Lambda^f(t,0)_{i,j} = \langle\hat{f}_i^\dagger(t)\hat{f}_j\rangle = \sum_{k,l} e^{i\epsilon_k t}A_{i,k}A_{j,l}\langle\hat{d}_k^\dagger\hat{d}_l\rangle, \tag{A20}$$

$$\Lambda^f(0,t)_{j,i} = \langle\hat{f}_j^\dagger\hat{f}_i(t)\rangle = \sum_{k,l} e^{-i\epsilon_l t}A_{j,k}A_{i,l}\langle\hat{d}_k^\dagger\hat{d}_l\rangle, \tag{A21}$$

$$\Lambda^f(0,0)_{j,j} = \langle\hat{f}_j^\dagger\hat{f}_j\rangle = \sum_{k,l} A_{j,k}A_{j,l}\langle\hat{d}_k^\dagger\hat{d}_l\rangle. \tag{A22}$$

With this we have all the ingredients we require to compute an OTOC. In the case of a thermal state or an eigenstate, the expressions in Eqs. (A19)–(A22) are greatly simplified since the occupation matrix in eigenmode space is diagonal. We consider a Gibbs state of the form

$$\rho = \frac{e^{-\beta\hat{H}}}{Z}. \tag{A23}$$

For thermal states we label the correlations with an additional β. The correlations in eigenmode space are well known with different sites decoupled and the occupation numbers following a Fermi-Dirac statistic with zero chemical potential

$$\Lambda_{k,l}^{d,\beta} = \langle\hat{d}_k^\dagger\hat{d}_l\rangle_\beta = \begin{cases} \frac{1}{1+e^{\beta\epsilon_k}}, & k = l \\ 0, & \text{otherwise.} \end{cases} \tag{A24}$$

In the next Appendix we describe how to use these expressions to compute the OTOC between two S^z operators on different sites.

APPENDIX B: OUT-OF-TIME ORDERED CORRELATIONS

The OTOC we compute in Sec. III relies on the computation of Eq. (15), or rewriting it here,

$$F(t) = \langle\hat{\sigma}_i^z(t)\hat{\sigma}_j^z\hat{\sigma}_i^z(t)\hat{\sigma}_j^z\rangle, \tag{B1}$$

where we have dropped the $x = |i - j|$ term in favor of expressing it as only a function of time. Evaluating this expression is the same as evaluating Eq. (13). For the following, it is easy to represent $\hat{n}_i(t) = \hat{f}_i^\dagger(t)\hat{f}_i(t)$. Substituting the Jordan-Wigner transformation definition,

$$F(t) = 16\left\langle\left(\hat{n}_i(t) - \frac{1}{2}\right)\left(\hat{n}_j - \frac{1}{2}\right)\left(\hat{n}_i(t) - \frac{1}{2}\right)\left(\hat{n}_j - \frac{1}{2}\right)\right\rangle. \tag{B2}$$

Expanding this and simplifying this using $\hat{n}_i(t)^2 = n_i(t)$ and the anticommutation rules shown in Eq. (A17), we can write

$$F(t) = 16\langle\hat{n}_i(t)\hat{n}_j\hat{n}_i(t)\hat{n}_j - \tfrac{1}{2}(\hat{n}_i(t)\hat{n}_j\hat{n}_i(t) + \hat{n}_j\hat{n}_i(t)\hat{n}_j) + \tfrac{1}{4}[\hat{n}_j\hat{n}_i(t) - \hat{n}_i(t)\hat{n}_j] + \tfrac{1}{16}\rangle. \tag{B3}$$

Using Eq. (B3), we can now use the definitions of our initial conditions on Λ^d to derive exact expressions for the OTOCs.

1. Product states

We consider our initial state as one constructed from the vacuum state such that

$$|\Psi\rangle = \prod_{j\in\mathbb{S}}\hat{f}_j^\dagger|0\rangle, \tag{B4}$$

where the cardinality of the set $\mathbb{S}$ represents the conserved number of fermions on the lattice, $\langle\hat{N}\rangle = \sum_j\langle\hat{f}_j^\dagger\hat{f}_j\rangle = |\mathbb{S}|$. This gives us an initial local occupation matrix of the form

$$\Lambda_{i,j}^f(0) = \langle\hat{f}_i^\dagger\hat{f}_j\rangle = \begin{cases} 1, & i = j \ \wedge i \in \mathbb{S} \\ 0, & \text{otherwise.} \end{cases} \tag{B5}$$

First consider the case that $\hat{\sigma}_j^z$ is selected such that $j \in \mathbb{S}$. Then, using $\hat{f}_j^\dagger|\psi\rangle = 0$ and Eq. (A17) we get

$$F(t) = 8|a_{i,j}(t)|^2\langle\hat{n}_i(t)\rangle - 8|a_{i,j}(t)|^2 + 1. \tag{B6}$$

Similarly if we assume $j \notin \mathbb{S}$ such that $\hat{f}_j|\psi\rangle = 0$, then we recover

$$F(t) = 1 - 8|a_{i,j}(t)|^2\langle\hat{n}_i(t)\rangle. \tag{B7}$$

Equations (B6) and (B7) reveal that the fundamental behavior of the OTOC relies on $|a_{i,j}(t)|^2$ and $\langle\hat{n}_i(t)\rangle$. The product state OTOC will have two effects coming together:

equilibration of $\langle \hat{n}_i(t) \rangle$ and the out-of-time anticommutation relation $|a_{i,j}(t)|^2$. This extra equilibration is expected to contribute to extra structure not present in the thermal case.

2. Thermal states

The thermal OTOC is computed similarly to the product state, but we exploit its simple structure in eigenmode space as seen in Eqs. (A24). Here, we exploit the fact that $\hat{f}_i^2 = \hat{f}_i^{\dagger 2} = 0$ and use Wicks theorem for thermal states [63]. This gives us the following form:

$$F(t) = 16|a_{i,j}(t)|^2 \big(\langle \hat{f}_i^\dagger \hat{f}_i \rangle_\beta \langle \hat{f}_j^\dagger \hat{f}_j \rangle_\beta - \tfrac{1}{2} (\langle \hat{f}_i^\dagger \hat{f}_i \rangle_\beta + \langle \hat{f}_j^\dagger \hat{f}_j \rangle_\beta) + \bar{a}_{i,j}(t) \langle \hat{f}_i^\dagger(t) \hat{f}_j \rangle_\beta - \langle \hat{f}_i^\dagger(t) \hat{f}_j \rangle_\beta \langle \hat{f}_j^\dagger \hat{f}_i(t) \rangle_\beta \big) + 1, \quad \text{(B8)}$$

where we have used the fact that same time two-point correlators are stationary, $\langle \hat{f}_i^\dagger(t) \hat{f}_i(t) \rangle_\beta = \langle \hat{f}_i^\dagger \hat{f}_i \rangle_\beta$. Equation (B8) is quite a bit more complicated than Eq. (B6), but the defining behavior is still reliant on $|a_{i,j}(t)|^2$ while the quantity $\langle \hat{n}_i(t) \rangle$ is now time independent. Instead, we see out-of-time correlations in the form of $\langle \hat{f}_j^\dagger \hat{f}_i(t) \rangle_\beta$, for example, play a role.

[1] J. Maldacena, S. H. Shenker, and D. Stanford, JHEP 08 (2016) 106.
[2] A. I. Larkin and Y. N. Ovchinnikov, Zh. Eksp. Teor. Fiz. **55**, 2262 (1969) [JETP **28**, 1200 (1969)].
[3] B. Swingle and D. Chowdhury, Phys. Rev. B **95**, 060201 (2017).
[4] X. Chen, T. Zhou, D. A. Huse, and E. Fradkin, Ann. Phys. **529**, 1600332 (2017).
[5] Y. Sekino and L. Susskind, JHEP 10 (2008) 065.
[6] S. Sachdev and J. Ye, Phys. Rev. Lett. **70**, 3339 (1993).
[7] S. Sachdev, Phys. Rev. X **5**, 041025 (2015).
[8] D. A. Roberts, D. Stanford, and L. Susskind, JHEP 03 (2015) 051.
[9] W. Fu and S. Sachdev, Phys. Rev. B **94**, 035135 (2016).
[10] J. Maldacena and D. Stanford, Phys. Rev. D **94**, 106002 (2016).
[11] B. Dóra and R. Moessner, Phys. Rev. Lett. **119**, 026802 (2017).
[12] Y. Huang, Y.-L. Zhang, and X. Chen, Ann. Phys. **529**, 1600318 (2017).
[13] K. Slagle, Z. Bi, Y.-Z. You, and C. Xu, Phys. Rev. B **95**, 165136 (2017).
[14] R. Fan, P. Zhang, H. Shen, and H. Zhai, Sci. Bull. **62**, 707 (2017).
[15] D.-L. Deng, X. Li, J. H. Pixley, Y.-L. Wu, and S. Das Sarma, Phys. Rev. B **95**, 024202 (2017).
[16] R. Nandkishore and D. A. Huse, Annu. Rev. Condens. Matter Phys. **6**, 15 (2015).
[17] F. Alet and N. Laflorencie, C. R. Phys. (to be published).
[18] D. J. Luitz and Y. Bar Lev, Phys. Rev. B **96**, 020406 (2017).
[19] S. Xu and B. Swingle, arXiv:1805.05376.
[20] S. Xu and B. Swingle, arXiv:1802.00801.
[21] S. Sahu, S. Xu, and B. Swingle, arXiv:1807.06086.
[22] S. H. Shenker and D. Stanford, JHEP 03 (2014) 067.
[23] Y. Gu, X.-L. Qi, and D. Stanford, JHEP 05 (2017) 125.
[24] A. A. Patel, D. Chowdhury, S. Sachdev, and B. Swingle, Phys. Rev. X **7**, 031047 (2017).
[25] D. Chowdhury and B. Swingle, Phys. Rev. D **96**, 065005 (2017).
[26] A. Nahum, S. Vijay, and J. Haah, Phys. Rev. X **8**, 021014 (2018).
[27] V. Khemani, A. Vishwanath, and D. A. Huse, Phys. Rev. X **8**, 031057 (2018).
[28] T. Rakovszky, F. Pollmann, and C. W. von Keyserlingk, Phys. Rev. X **8**, 031058 (2018).
[29] H. Liu and S. J. Suh, Phys. Rev. Lett. **112**, 011601 (2014).
[30] P. Hosur, X.-L. Qi, D. A. Roberts, and B. Yoshida, JHEP 02 (2016) 004.
[31] N. Yunger Halpern, Phys. Rev. A **95**, 012120 (2017).
[32] N. Yunger Halpern, B. Swingle, and J. Dressel, Phys. Rev. A **97**, 042105 (2018).
[33] J. R. G. Alonso, N. Yunger Halpern, and J. Dressel, Phys. Rev. Lett. **122**, 040404 (2019).
[34] J. H. Bardarson, F. Pollmann, and J. E. Moore, Phys. Rev. Lett. **109**, 017202 (2012).
[35] M. Serbyn, Z. Papić, and D. A. Abanin, Phys. Rev. Lett. **110**, 260601 (2013).
[36] M. Žnidarič, T. Prosen, and P. Prelovšek, Phys. Rev. B **77**, 064426 (2008).
[37] G. D. Chiara, S. Montangero, P. Calabrese, and R. Fazio, J. Stat. Mech. (2006) P03001.
[38] H. Abdul-Rahman, B. Nachtergaele, R. Sims, and G. Stolz, Lett. Math. Phys. **106**, 649 (2016).
[39] F. Iglói, Z. Szatmári, and Y.-C. Lin, Phys. Rev. B **85**, 094417 (2012).
[40] W. Son, L. Amico, F. Plastina, and V. Vedral, Phys. Rev. A **79**, 022302 (2009).
[41] A. Nahum, J. Ruhman, and D. A. Huse, Phys. Rev. B **98**, 035118 (2018).
[42] M. McGinley, A. Nunnenkamp, and J. Knolle, Phys. Rev. Lett. **122**, 020603 (2019).
[43] C. W. von Keyserlingk, T. Rakovszky, F. Pollmann, and S. L. Sondhi, Phys. Rev. X **8**, 021013 (2018).
[44] A. Bohrdt, C. B. Mendl, M. Endres, and M. Knap, New J. Phys. **19**, 063001 (2017).
[45] R. J. Lewis-Swan *et al.*, arXiv:1808.07134.
[46] C. Murthy and M. Srednicki, arXiv:1809.03681.
[47] M. Gluza, J. Eisert, and T. Farrelly, arXiv:1809.08268.
[48] C.-J. Lin and O. I. Motrunich, Phys. Rev. B **97**, 144304 (2018).
[49] S. Byju, K. Lochan, and S. Shankaranarayanan, arXiv:1808.07742.
[50] C.-J. Lin and O. I. Motrunich, Phys. Rev. B **98**, 134305 (2018).
[51] E. Hamza, R. Sims, and G. Stolz, Commun. Math. Phys. **315**, 215 (2012).
[52] P. Coleman, *Introduction to Many-Body Physics* (Cambridge University Press, Cambridge, UK, 2015).
[53] J. Riddell and M. P. Müller, Phys. Rev. B **97**, 035129 (2018).
[54] H.-H. Lai and K. Yang, Phys. Rev. B **91**, 081110 (2015).

[55] H. Abdul-Rahman, B. Nachtergaele, R. Sims, and G. Stolz, Ann. Phys. **529**, 1600280 (2017).
[56] G. Stolz, Contemp. Math. **552**, 71 (2011).
[57] W. Miller, *Symmetry Groups and Their Applications*, Computer Science and Applied Mathematics (Academic, New York, 1972).
[58] I. Peschel and V. Eisler, J. Phys. A: Math. Theor. **42**, 504003 (2009).
[59] M. Pouranvari, Y. Zhang, and K. Yang, Adv. Condens. Matter Phys. **2015**, 4 (2015).
[60] J. I. Latorre and A. Riera, J. Phys. A: Math. Theor. **42**, 504002 (2009).
[61] M. Perarnau-Llobet, A. Riera, R. Gallego, H. Wilming, and J. Eisert, New J. Phys. **18**, 123035 (2016).
[62] C. Gramsch and M. Rigol, Phys. Rev. A **86**, 053615 (2012).
[63] M. Gaudin, Nucl. Phys. **15**, 89 (1960).